HHS Public Access

Author manuscript

Nat Med. Author manuscript; available in PMC 2014 December 01.

Published in final edited form as:

Nat Med. 2014 June ; 20(6): 624–632. doi:10.1038/nm.3543.

Cardiac Spliced BIN1 Folds T-tubule Membrane, Controlling Ion Flux and Limiting Arrhythmia

TingTing Hong[1,*], **Huanghe Yang**[2,*], **Shan-Shan Zhang**[1], **Hee Cheol Cho**[1], **Mariya Kalashnikova**[1], **Baiming Sun**[1], **Hao Zhang**[3], **Anamika Bhargava**[4], **Michael Grabe**[3], **Jeffrey Olgin**[5], **Julia Gorelik**[4], **Eduardo Marbán**[1], **Lily Y. Jan**[2,3,6], and **Robin M. Shaw**[1,†]

[1]Cedars-Sinai Heart Institute, Cedars-Sinai Medical Center, Los Angeles, CA, USA

[2]Departments of Physiology, Biochemistry and Biophysics, University of California San Francisco, San Francisco, CA, USA

[3]Cardiovascular Research Institute, University of California San Francisco, San Francisco, CA, USA

[4]Imperial Center for Translational and Experimental Medicine, Imperial College, London, UK

[5]Division of Cardiology, Department of Medicine, University of California San Francisco, San Francisco, CA, USA

[6]Howard Hughes Medical Institute, USA

Abstract

Cardiomyocyte T-tubules are important for regulating ionic flux. Bridging Integrator 1 (BIN1) is a T-tubule protein associated with calcium channel trafficking that is down-regulated in failing hearts. Here we find that cardiac T-tubules normally contain dense protective inner membrane folds that are formed by a cardiac spliced isoform of BIN1. In mice with cardiac *Bin1* deletion, T-tubule folding is decreased which does not change overall cardiomyocyte morphology, but frees diffusion of local extracellular calcium and potassium ions, prolonging action potential duration, and increasing susceptibility to ventricular arrhythmias. We also find that T-tubule inner folds are rescued only by the BIN1 isoform BIN1+13+17, which promotes N-WASP dependent actin polymerization to stabilize T-tubule membrane at cardiac Z-discs. In conclusion, BIN1+13+17 recruits actin to fold T-tubule membrane, creating a fuzzy space that protectively restricts ionic

†To whom correspondence should be addressed: Robin M. Shaw, MD, PhD, Cedars-Sinai Heart Institute, CSMC, Davis Bldg., Room #1016, 8700 Beverly Blvd, Los Angeles, CA 94048, robin.shaw@cshs.org, Phone: (310) 967-3842, Fax: (310) 967-3891.

*These authors contributed equally to this work.

AUTHOR CONTRIBUTIONS

All authors contributed to study design, analysis of the data, and writing of the paper. T.T.H. was involved in the design and performance of all key experiments, H.Y. did the patch clamp experiments, S.Z. prepared mouse crossing, adenovirus and *Bin1* cloning experiments, H.C.C. and B.S. did the in vivo arrhythmia experiments, M.K. performed the actin polymerization assay, A.B. did the SICM imaging and analysis of T-tubule topology, H.Z. did the optical mapping studies, M.G. did the mathematical modeling.

The authors have no competing interests as defined by Nature Publishing Group, or other interests that might be perceived to influence the results and/or discussion reported in this paper.

flux. When BIN1+13+17 is decreased, as occurs in acquired cardiomyopathy, T-tubule morphology is altered and arrhythmias can result.

Cardiac T-tubules are highly-branched invaginations of cardiomyocyte sarcolemma. T-tubules are primarily transverse to the cardiomyocyte long axis and wrap around sarcomeric Z-discs[1]. As an organelle involved in the initiation of calcium transients[2], the T-tubule system helps determine the strength of each heartbeat by concentrating L-type calcium channels (LTCCs) and positioning them in close proximity with ryanodine receptors at the sarcoplasmic reticulum (SR)[2–4]. The lumina of T-tubules are continuous with the extracellular milieu which is calcium-rich. During each heartbeat, an action potential triggers extracellular calcium entry into the cell through LTCCs, increasing local intracellular calcium, activating nearby ryanodine receptors, and inducing large calcium release from intracellular SR stores, resulting in cellular contraction. Thus, T-tubules help regulate efficient beat-to-beat calcium flux.

There is growing appreciation that diffusion between the T-tubule lumen and bulk extracellular space is restricted[5–8]. Even though T-tubule lumina have an overall wide diameter of 20–450 nm[1], they may only be accessible to ions and small nano-particles (≤11 nm)[9]. T-tubule diffusion coefficients for extracellular ions are ~95 $\mu m^2/s$ for calcium ions[7], and ~85 $\mu m^2/s$ for potassium ions, which are five to ten times slower than in bulk extracellular space[8]. At fast heart rates, rapid transmembrane flux and limited diffusion can result in depleted T-tubule lumen calcium[5,10] and elevation of T-tubule lumen potassium[8], affecting the driving force for trans-membrane ion flux and decreasing action potential duration[11].

The current understanding of T-tubule structures includes recognition of large branch points within the T-tubule lumen[1], but does not explain highly-restricted diffusion. Furthermore, in failing hearts, T-tubule remodeling is notable for even larger yet fewer T-tubules[12–14]. Also, in failing hearts, action potentials are prolonged[15] and intracellular calcium overload occurs[16], resulting in dangerous arrhythmias[16]. Action potential duration and calcium handling are strongly influenced by T-tubule-associated currents, but without a better understanding of T-tubule anatomy, it remains difficult to clarify the impact of T-tubules on cardiac electrophysiology or determine the impact of altered T-tubules in disease.

Recent studies suggest that the membrane scaffolding protein Bridging Integrator 1 (BIN1) can be a regulator of T-tubule structure and function. BIN1, a member of the BAR domain containing protein superfamily, can induce LTCC-enriched membrane folds in cell lines and immature muscle cells[17,18]. In adult cardiomyocytes, BIN1 localizes to cardiac T-tubules and facilitates cytoskeleton-based calcium channel trafficking to T-tubule membrane[18]. The expression of BIN1 is transcriptionally decreased in acquired human and animal heart failure, which is also associated with both intracellular accumulation of LTCCs and abnormal T-tubule morphology[12,13,19,20]. A case of ventricular arrhythmias associated with BIN1 mutation has been reported[21].

In the present study, the anatomy and function of cardiac T-tubules were studied in young adult mice with or without cardiac deletion of *Bin1*. With complementary *in vivo* and *ex vivo*

studies, imaging, electrophysiology, biochemistry, and mathematical modeling, we find that an alternatively-spliced cardiac isoform of BIN1, BIN1+13+17, exists in mouse heart, promotes N-WASP-dependent actin polymerization and is responsible for generating actin-organized and densely-packed T-tubule membrane folds. The folds create a physical diffusion barrier to extracellular ions and protect against arrhythmias. Our finding elucidates how cardiac T-tubule ionic concentrations can differ from bulk extracellular ionic composition, and why the T-tubule diffusion barrier disappears in heart failure, increasing the likelihood of ventricular arrhythmias.

RESULTS

Cardiomyocyte T-tubule membrane is densely folded by BIN1

Homozygous mice with global *Bin1* deletion suffer perinatal death due to cardiomyopathy[22]. To explore the role of BIN1 in cardiac T-tubule organization, we generated a cardiac-specific deletion of *Bin1* using α-myosin heavy chain α*MHC-Cre*$^{+}$[23] and loxP-flanked *Bin1* lines to generate heterozygous (*Bin1* HT, *Bin1*$^{flox/+}$; α*MHC-Cre*$^{+}$) and homozygous (*Bin1* HO, *Bin1*$^{flox/flox}$; α*MHC-Cre*$^{+}$) mice. Use of the α*MHC-Cre* bypasses embryonic lethality[24]. At 8–12 weeks, the wildtype (WT), *Bin1* HT (reduction in BIN1 similar to that in heart failure[19]) and *Bin1* HO animals have similar overall body and heart phenotypes (Supplementary Figs. 1 and 2), consistent with high cardiac reserve typical for young adult hearts[24]. Adult cardiomyocytes were isolated from the WT and *Bin1* HT animals and labeled with a plasma membrane lipid dye Di-8-ANNEPs for live-cell imaging by spinning disk confocal microscopy (Fig. 1a–c and Supplementary Fig. 3). We found that the distribution and regularity of T-tubules are preserved in cardiomyocytes from *Bin1* HT hearts. However, T-tubule fluorescence is decreased in the *Bin1* HT cells, indicating less membrane along T-tubule invaginations. Similar results were obtained when membrane structures of freshly-fixed cardiomyocytes were labeled with wheat germ agglutinin (WGA, Supplementary Fig. 3b). Electrophysiological measurement of cardiomyocyte T-tubule capacitance, which is 30% of total cardiomyocyte capacitance[25], is decreased by 46% in *Bin1* HT (Fig. 1d) cells with normal cell size (Supplementary Fig. 3c), confirming decreased T-tubule membrane in the cardiomyocytes that are deficient in BIN1. The decrease in T-tubule membrane occurs despite preserved cellular content of T-tubule proteins (Supplementary Fig. 4a).

To directly visualize the impact of *Bin1* deletion on T-tubule membrane *in situ*, we used transmission electron microscopy (TEM, Fig. 1e–h). Freshly-isolated whole mouse hearts were perfused with a calcium-containing fixative, and the left ventricular free wall was then sectioned and post-fixed with potassium ferricyanide, which enhances membrane contrast by forming calcium-dependent extracellular precipitates[26,27]. We found that the gross morphology of T-tubule invaginations is preserved in *Bin1* HT and HO cardiomyocytes (Fig. 1e, left). In the high-magnification transverse and axial cross sectional images of T-tubules (Fig. 1e, quantification in 1f), we observed that, relative to WT T-tubules, *Bin1* HT T-tubules consistently have fewer calcium-dense membrane folds. As revealed by 3D tomography (Fig. 1e, right panel), these membrane folds divide WT T-tubule lumen into multiple spatial subdomains, which are lost in the *Bin1* HT and *Bin1* HO T-tubules. As a result, *Bin1* HT and *Bin1* HO T-tubules contain one singular luminal space, which is

enlarged in *Bin1* HO cardiomyocytes (quantification in Fig. 1g). To numerically compare the degree of contoured T-tubules between WT and non-dilated *Bin1* HT T-tubules, we applied a T-tubule contour score to each axial cross section image of T-tubule from multiple samples (three sections per heart and two hearts per genotype), assigning a score of 1 (round T-tubule lumen without folds and spatial complexity), 2 (non-circular contoured T-tubule lumen without folds and spatial complexity), or 3 (both round and non-circular T-tubules with multiple folds and spatial complexity). We found that T-tubules in *Bin1* HT cardiomyocytes are dramatically less contoured and folded (Fig. 1h). Consistent with these findings, T-tubule topology by scanning ion conductance microscopy reveals more distinct T-tubule openings with large diameters in *Bin1* HT cardiomyocytes, indicating that BIN1-folded membrane creates a “fuzzy space” inside T-tubules (Supplementary Fig. 3d).

BIN1 determines the T-tubule ion diffusion barrier

What is the function of T-tubule membrane folds? One possibility, suggested by the calcium density, is that the folds create an extracellular microenvironment distinct from the bulk extracellular space. We measured the dynamics of calcium ion diffusion into T-tubules by recording the I_{Ca} current through LTCCs while rapidly changing extracellular calcium. The baseline measurements revealed that *Bin1* HT cardiomyocytes have similar total protein expression level of Cav1.2 (Supplementary Fig. 4a) and, of the membrane-inserted channels, preserved preferential localization of LTCCs to T-tubules. The *Bin1* HT cardiomyocytes also have less total membrane LTCCs and less overall LTCC current (Supplementary Fig. 4b), consistent with our previous report that BIN1 helps LTCC forward trafficking[18]. Next, the activity of the surface LTCCs was studied by recording I_{Ca} decay kinetics following a rapid switch of extracellular perfusate from physiological calcium concentration to zero calcium (buffered with 5 mM EGTA; Fig. 2a). After an initial delay, I_{Ca} decayed exponentially until all extracellular calcium inside the T-tubules was removed or chelated (Fig. 2b). In *Bin1* HT cardiomyocytes, the time length of the initial delay (X_0) is shortened by 64 ms compared to that of WT cardiomyocytes (239 ± 5 ms vs. 303 ± 10 ms, Fig. 2c, P = 0.0001). To test whether shortened X_0 could be due to increased ion diffusion within the T-tubules, a simple mathematical model of calcium diffusion was implemented containing a slow diffusion zone (T-tubule folds, Fig. 1eh), a rapid diffusion zone (T-tubule central lumen, tomography in Fig. 1e) and EGTA chelation (Fig. 2d). The theoretical decay curve generated from the model superimposes with the experimental data in WT cardiomyocytes. Removal of the diffusion barrier results in a shortened X_0, as seen in the *Bin1* HT cardiomyocytes (Fig. 2e). The autonomous mathematical algorithm that determined best-fit T-tubule diffusion and anatomical parameters yielded values that are remarkably consistent with those previously measured (Supplementary Table 1), providing computational support for a model of BIN1-induced restricted extracellular calcium diffusion.

Next, we asked whether the physical barrier formed by BIN1-organized membrane folds applies to other ions. With regard to potassium ions, which can also be affected by slow diffusion[8], we measured current from the inwardly rectifying potassium channel, I_{K1}, which maintains the cardiomyocyte resting membrane potential. As indicated in Fig. 3a, steady-state I_{K1} and its kinetics were recorded following rapid wash-in and wash-out of K^+ in T-tubules. Similar to our observations of calcium diffusion, decay of I_{K1} in response to an

increase of extracellular potassium concentration from 5 mM to 8.1 mM (K^+_{on}) is significantly faster in *Bin1* HT cardiomyocytes (Fig. 3b, c). The smaller difference of K^+ diffusion (24 ms versus 64 ms for calcium) between WT and *Bin1* HT likely reflects less T-tubule based enrichment of I_{K1}[28,29]. Similarly, I_{K1} response to decreases of extracellular potassium concentration from 8.1 mM back to 5 mM (K^+_{off}) is also significantly faster in *Bin1* HT cardiomyocytes (Fig. 3d, e).

A change in extracellular diffusion will affect the extracellular ion concentration, altering ion channel activity and electrophysiological parameters. We recorded electrocardiograms (EKGs) and performed whole-heart optical mapping on both WT and *Bin1* HT hearts. In *Bin1* HT hearts, action potentials are prolonged and ectopy from afterdepolarizations occurs both spontaneously and with induction (Fig. 3f). If limited diffusion includes an increase in extracellular potassium of the local fuzzy space, then in theory hyperkalemia will induce sodium channel block and conduction failure in WT animals before HT animals[30]. When the hearts were perfused with high-potassium solution, fast pacing induced conduction block more readily in WT than in HT hearts (Fig. 3g). These data support a difference in extracellular potassium accumulation in WT versus HT hearts.

Bin1 HT and HO mice have inducible ventricular arrhythmias

Given the effects of BIN1 reduction on ion homeostasis and membrane potential prolongation, we next studied *in vivo* arrhythmogenesis in WT, *Bin1* HT and *Bin1* HO mice subjected to ventricular pacing before and after intra-myocardial injection of isoproterenol. As is evident from the representative EKG recordings (Fig. 4a), sinus rhythm resumes immediately after ectopic pacing in WT mice (top panel). However, sustained monomorphic ventricular tachycardia (VT) ensues after pacing in *Bin1* HT mice (middle panel), and more severe sustained polymorphic VT alternating with ventricular fibrillation (VF) occurs in *Bin1* HO mice (bottom panel). The overall incidence of sustained VT (>9 consecutive wide-complex beats)[31,32] or VF (Fig. 4c), as well as the frequency of pacing-induced arrhythmias (Fig. 4d), were significantly increased in *Bin1* HT and HO mice. *Bin1* deletion also dramatically increased isoproterenol-induced arrhythmias (Fig. 4d), which have been linked to LTCC-mediated afterdepolarizations[33].

BIN1+13+17 uses F-actin to maintain T-tubule folds at Z-discs

To identify the BIN1 isoform(s) responsible for T-tubule membrane folding, we explored cardiac splicing of *Bin1*, which is a gene encoded by 20 exons (Fig. 5a). Using PCR detection and sequencing of cloned fragments with primers flanking the alternatively spliced region between exon 10 (or exon 13) and 18 (Fig. 5b,c), we found that *Bin1* message in adult mouse cardiomyocytes consists of ubiquitous *Bin1* (36% of all clones) and *Bin1+17* (8%), as well as the alternatively-spliced cardiac variants *Bin1+13* (48%) and *Bin1+13+17* (8%). Quantitative rt-PCR confirms a similar expression pattern and further identifies an increase of gene expression of all the *Bin1* variants in mature adult mouse cardiomyocytes relative to neonatal cardiomyocytes (Fig. 5d). Next, we used exon 13- or 17-specific BIN1 antibodies (Fig. 5e) to localize the distribution of BIN1 isoforms in adult mouse cardiomyocytes. Both anti-BIN1–13 and anti-BIN1–17 antibodies localized to anti-α-actinin

and anti-Cav1.2 identified Z-line/T-tubules regions (Fig. 5f), indicating that BIN1+13+17 resides at T-tubules.

The localization of BIN1+13+17 to T-tubules indicates a role in organizing membrane folds. Imaging of T-tubules indicates that exogenous BIN1+13+17 is the only isoform capable of fully rescuing T-tubule membrane intensity in *Bin1* HT cardiomyocytes (Fig. 5g and Supplementary Fig. 5a). Conversely, in WT adult mouse cardiomyocytes, *Bin1* knockdown using lentivirus-mediated shRNA targeting constitutive exon 2 or exon 13 decreases T-tubule membrane intensity, in proportion to BIN1 protein reduction (Supplementary Fig. 5b).

To understand how BIN1+13+17 organizes T-tubule membrane, we expressed GFP-tagged BIN1 isoforms in HeLa cells. Both confocal and TEM (Fig. 6a–c) imaging identified that only BIN1+13+17 induces formation of elongated, F-actin associated, membrane folds (Fig. 6d), indicating a role of actin in BIN1+13+17-mediated fold formation. Cytochalasin D induced stabilization of the barbed ends of F-actin at Z-discs is known to help preserve T-tubule structure of cultured cardiomyocytes[34]. We found that actin stabilization by cytochalasin D increases, whereas actin disruption by latrunculin A decreases, cardiac T-tubule membrane intensity (Supplementary Fig. 6). To further explore the differential roles of BIN1 isoforms in organizing actin, we studied their interaction with the actin polymerizing protein N-WASP, a known binding partner of the BAR domain protein Amphiphysin 1[35]. Interestingly, although BIN1+13 does not bind to N-WASP (Fig. 6e), BIN1+13+17 does and can activate N-WASP to promote Arp2/3 nucleated actin polymerization (Fig. 6f). Biochemical GST pull-down confirms that BIN1+13+17 is associated with F-actin and α-actinin in adult mouse hearts (Fig. 6g). These data indicate that BIN1+13+17 binds to and activates N-WASP function to form elongated F-actin polymers for the development of membrane folds, and binds to Z-disc α-actinin to maintain these membrane folds, creating an ionic diffusion barrier within cardiac T-tubules (cartoon in Fig. 6h).

DISCUSSION

Here we report that cardiac T-tubules are densely folded by a particular cardiac isoform of BIN1, resulting in local extracellular microenvironments that resist diffusion with bulk extracellular space with important consequences for membrane electrophysiology. The results expand the repertoire of BIN1 proteins to include a role for alternative splicing and cytoskeleton-based membrane localization to fold T-tubule membrane and regulate ionic flux. In conditions where cardiac BIN1 is transcriptionally decreased, such as heart failure[19,20], the loss of a T-tubule fuzzy space in failing cardiomyocytes can increase arrhythmogenesis[16,36]. Our studies indicate that a loss of BIN1 increases arrhythmogenesis independent of the organ level structural changes that are associated with failing hearts.

Our results provide the first direct experimental evidence for the presence of a “slow diffusion zone”, or “fuzzy space” that has been proposed previously[6], inside the T-tubule network. Future consideration of cardiomyocyte electrophysiology should take into account a separate slow diffusion zone at the inner face of T-tubules organized by membrane folds.

The two zones separated by a resistant barrier have been predicted from computer models to change action potential duration[11], and increase the safety of spatial propagation of cardiac action potentials[37]. Consistently, we found that removal of the BIN1-organized "fuzzy space" prolongs action potential duration and increases ventricular arrhythmias. Removal of the ion diffusion barrier also significantly increases cardiac sensitivity to β adrenergic receptor activation. Thus, by creating a physical barrier that impedes the access of particles[9] such as catecholamine, the folded T-tubules serve as a protective mechanism to maintain cardiomyocyte homeostasis when extracellular bulk environment fluctuates. It remains unclear how the T-tubule folding affects efficient calcium-induced-calcium-release (CICR). The folds could in theory bring LTCCs closer to nearby ryanodine receptors. A recent study also suggests a direct conformational change of calcium binding activated LTCC, a mechanism in addition to local Ca^{2+} diffusion, may help cardiac CICR similar to the known mechanism of skeletal CICR[38]. Future studies of intracellular ion diffusion, and the relationship between channel density and the folds supporting the channels, in *Bin1*-depleted cardiomyocytes could enhance our understanding of calcium cycling.

Our study adds a cardiac-specific context to *Bin1* splicing. The exon 1316 encoded clathrin binding domain targets neuronal BIN1 to clathrin-coated pits, facilitating endocytosis[39] and neurotransmitter reuptake[40]. Exon 11 inclusion encodes a phosphoinositide binding domain that targets skeletal BIN1 to the plasma membrane for skeletal tubular biogenesis[17]. We found inclusion of exons 13 and 17 targets BIN1+13+17 to cardiac T-tubules for extensive membrane folding. This cardiac-specific, isoform-dependent function of BIN1 involves N-WASP-mediated actin polymerization, helping BIN1+13+17 to extend F-actin organized membrane folds. Through α-actinin binding, BIN1+13+17 stabilizes these folds at cardiac Z-discs. It may be that, in addition to skeletal tubulogenesis[17], BIN1+11+17 has an analogous maintenance role in skeletal muscle[41], but given the significant differences in T-tubule number, size, and location in skeletal versus cardiac muscle, careful studies are needed in each muscle subtype.

Other functions of the cardiac-expressing BIN1 isoforms, unrelated to T-tubule folding, are likely. Constitutive knockout of BIN1 causes embryonic cardiac hypertrophy and lethality[22], occurring before postnatal T-tubule development. Our cardiac-specific *Bin1* HO mice used the α-MHC promoter driven Cre which, in ventricular myocytes, activates in the perinatal stage. Furthermore, the most abundant cardiac isoform of BIN1 is BIN1+13, which elsewhere is associated with cell proliferation[42]. It is interesting that this isoform does not interact with actin but localizes to actin-free M-line regions. Given BIN1 has been implicated in roles as varied as endocytosis to transcription co-factor[43,44], future studies will be helpful to define the spectrum of roles of different BIN1 isoforms in the heart.

In conclusion, we find that cardiac T-tubules are densely folded by a particular BIN1 isoform, resulting in retention of extracellular ions that are protective of heart function during stress by modulating transmembrane ion flux. We previously found that BIN1 anchors microtubules to deliver LTCCs to T-tubule membrane[18]. The present findings indicate that BIN1 can also create T-tubule folds to which the channels can be delivered. When BIN1 and other scaffolding proteins are reduced, such as in heart failure[14,19,45], not only are potential membrane anchor points lost, the membrane fold itself is no longer

present. Loss of the folds can help explain the increase in ventricular arrhythmias that occur in failing hearts[46].

ONLINE METHODS

Plasmids, antibodies, and cell culture

Rabbit polyclonal antibody (A#5299, Anaspec) was raised against BIN1 peptide LRKGPPVPPPPKHTPSKEMKQEQI (epitope encoded by exon 13). We also used antibodies directed against the exon 17 encoded MYC-binding domain of BIN1 (99D, Sigma), pan-BIN1 rabbit antibody against SH3 domain (Abcam), mouse and rabbit anti α-actinin (Abcam), rabbit anti Cav1.2 (Alomone), mouse and rabbit anti V5 (Sigma), rabbit anti actin (Sigma), rabbit anti GST (Santa Cruz Inc.).

LifeAct-mCherry was described previously[47]. Bovine N-WASP was obtained from Addgene (Plasmid 33019: Pcs2-Bnwasp). HeLa and FT293 cells were cultured in DMEM under standard mammalian cell conditions. Lipofectamine 2000 (Invitrogen) was used for cDNA transfections in HeLa cells.

Cloning

Total RNA was extracted from isolated mouse cardiomyocytes and reverse transcribed into cDNA using iScript™ cDNA synthesis kit (BioRad). The resulting cDNA was used for PCR amplification of the middle section including alternatively spliced region using the following two primer sets: for exon 10–18 TTCACAGTCAAGGCCCAACC (Fwd) and ACCACCACAGCCGGAAGAGA (Rev); and for exon 13–18: TCCCCAAGTCCCCATCTCA (Fwd) and ACCACAGCCGGAAGAGAGCT (Rev). To further confirm the sequence, the first set of primers (exon 10–18) flanked with attB1/attB2 sites were used to PCR out the same regions for subsequent Gateway BP cloning into pDONR/Zeo (Invitrogen) to generate entry clones. A total of one hundred entry clones of the cardiac *Bin1* middle section (exon 10–18, $n = 100$) were sequenced to identify a total of 4 distinct isoforms expressed in cardiomyocytes. The percent of clones of each variant was also analyzed and presented in Fig. 5c.

Meanwhile, to obtain *Bin1* expression clones, full length *Bin1* genes were amplified using primers flanked with attB1/attB2 sites. The PCR products were BP cloned into pDONR/Zeo construct to generate entry clones. The entry clones were sequenced to obtain all four cardiac BIN1 isoforms, which were subsequently inserted into pDest-eGFP-N1, pDest-mCherry-N1 (converted vectors originally from Clontech), pcDNA3.2-V5-Dest, pDest27-N-GST, and pAdeno-V5-Dest by Gateway LR cloning to generate final tagged expression clones and adenovirus.

qRT-PCR analysis of cardiac *Bin1* variants in isolated adult and neonatal mouse cardiomyocytes

Adult mouse cardiomyocytes were isolated from 8 week old C57/B6 mouse hearts according to a previously established method[48]. The stepwise calcium reintroduction and slow centrifugation (40 *g*) followed by plating on laminin pre-coated dishes were used to generate

a population of adult mouse cardiomyocytes with 90% as viable rod shape cells[48]. Following neonatal (P3) cardiomyocyte isolation[18], we adopted an efficient non-genetic mitochondrial labeling approach using flow cytometry[49] (BD Biosciences LSRII and FACSAriaII) to separate cardiomyocytes with the highest mitochondrial dye intensity, which were further confirmed with cardiac marker (Tnni3 and MF20) expression. Total RNA was then isolated from purified adult and neonatal cardiomyocytes using Picopure RNA extraction kit (Arcturus), and cDNA was synthesized using the BioRad iScript™ kit. To determine mRNA expression level of cardiac *Bin1* variants, we designed exon junction-specific primers to quantify splice variant levels by qRT-PCR at both P3 neonatal and adult mouse cardiomyocytes. Custom Taqman exon-specific primers were generated to span exon junctions of interest (12 and 13, 17 and 18, 12 and 17, 12 and 18) using the Custom TaqMan® Assay Design Tool to ensure specificity without repeats or SNPs. Assay A uses exon12 and 13 junction to detect *Bin1+13* and *Bin1+13+17*; Assay B uses exon 17 and 18 junction to detect both *Bin1+17* and *Bin1+13+17*; Assay C uses exon 12 and 17 junction to detect only *Bin1+17*; and Assay D uses exon 12 and 18 junction to detect only the smallest *Bin1* variant. The expression level of *Bin1+13+17* is derived by Assay B-C, and the expression level of *Bin1+13* is estimated by A-(B-C). The custom probe sequences are:

Bin1_12_13
TGACAATGCCCCTGAGAAAGGGAACAAGAGCCCGTCACCTCCTCCAGATGGCTC
CCCTGCTGCTACCCCTGAGATCAGAGTGAACCATGAGCCAGAGCCGGCCAGTGG
GGCCTCACCCGGGGCTACCATCCCCAAGTCCCCATCTCAGCTCCGGAAAGGCCC
ACCTGTCCCTCCGCCTCCCAAACACACCCCATCCAAGGAGATGAAGCAGGAGCA
GATTCTCAGCCTTTTTGATGACGCATTTGTCCCTGAGATCAGCGTGACCACCCCC
TCCCAG 94=ex11, 204=ex12

Bin1_12_17
TGACAATGCCCCTGAGAAAGGGAACAAGAGCCCGTCACCTCCTCCAGATGGCTC
CCCTGCTGCTACCCCTGAGATCAGAGTGAACCATGAGCCAGAGCCGGCCAGTGG
GGCCTCACCCGGGGCTACCATCCCCAAGTCCCCATCTCAGCCAGCAGAGGCCTC
CGAGGTGGTGGGTGGAGCCCAGGAGCCAGGGGAGACAGCAGCCAGTGAAGCA
ACCTCC 94=ex11,190=ex16

Bin1_17_18
CCAGCAGAGGCCTCCGAGGTGGTGGGTGGAGCCCAGGAGCCAGGGGAGACAGC
AGCCAGTGAAGCAACCTCCAGCTCTCTTCCGGCTGTGGTGGTGGAGACCTTCTC
CGCAACTGTGAATGGGGCGGTGGAGGGCAGCGCTGGGACTGGACGCTTGGACC
TGCCCCCGGGATTCATGTTCAAG 31=ex16, 141=ex17

Bin1_12_18
TGACAATGCCCCTGAGAAAGGGAACAAGAGCCCGTCACCTCCTCCAGATGGCTC
CCCTGCTGCTACCCCTGAGATCAGAGTGAACCATGAGCCAGAGCCGGCCAGTGG
GGCCTCACCCGGGGCTACCATCCCCAAGTCCCCATCTCAGAGCTCTCTTCCGGCT
GTGGTGGTGGAGACCTTCTCCGCAACTGTGAATGGGGCGGTGGAGGGCAGCGCT
GGGACTGGACGCTTGGACCTGCCCCCGGGATTCATGTTCAAG 94=ex11,203=ex17

Generation of the cardiac-specific *Bin1* heterozygote mouse and cardiomyocytes isolation

All mouse procedures were reviewed and approved by the University of California and Cedars-Sinai Medical Center IACUC (Institutional Animal Care and Use Committee). Heterozygote *Bin1flox* (loxP sites around exon 3 of the *Bin1* gene) mice were interbred with α*MHC-Cre* mice[23] to generate cardiomyocyte specific *Bin1* heterozygotes (*Bin1* HT, $Bin1^{flox/+}$; α*MHC- Cre*$^{+}$) and homozygotes (*Bin1* HO, $Bin1^{flox/flox}$; α*MHC-Cre*$^{+}$) (See detailed breeding strategies in Supplementary Fig.1). There are no differences in the other genotypes in the same litters ($Bin1^{+/+}$; *Cre*$^{-}$, $Bin1^{+/+}$; *Cre*$^{+}$, $Bin1^{flox/+}$; *Cre*$^{-}$, and $Bin1^{flox/flox}$; *Cre*$^{-}$) and hence data are pooled as wildtype (WT). Genotypes were confirmed by PCR to differentiate $Bin1^{+}$, $Bin1^{flox}$, and *Cre*$^{+}$ alleles. To confirm the efficiency of Cre-mediated deletion of *Bin1*, quantitative real-time PCR using TaqMan primer/probe sets (5'FAM/ 3'BHQ; Applied Biosystems) spanning constitutively splice exons 2 and 3 (Mm01158690_mH) was used to measure transcription of total *Bin1* gene, the house-keeping gene *Hrpt1*, and a cardiac specific gene *TnI3* in cardiomyocyte cDNA generated from both WT and *Bin1* HT mice. Quantitative real-time PCR reactions (qRT-PCR, 10 μl) were performed in a 384-well format using mix (Applied Biosystems) on an ABI 7900HT (Applied Biosystems).

Ventricular myocytes were isolated from 8–12 week old WT and *Bin1* HT littermates after dissociation with collagenase II (2 mg ml^{-1}, Worthington) using a previously described method[48]. Each cellular experiment represents cardiomyocytes isolated from three male and female (sex matched) mice per genotype.

Adenoviral and lentiviral infection of adult mouse cardiomyocytes

For rescue experiments, after 2 h plating, *Bin1* HT cardiomyocytes were infected with GFP or BIN1 isoform overexpressing adenovirus (MOI 1000) overnight for live-cell membrane imaging with Di-8-ANNEPS or fixed in 4% PFA and labeled with Alexa647 conjugated WGA for fixed cell membrane imaging. For *Bin1* knockdown experiments, cardiomyocytes were infected with (MOI 5) control, constitutive exon 2 BIN1 shRNA (5'–CCGGAGACGAAGGACGAGCAGTTTGCTCGAGCAAACTGCTCGTCCTTCGTCTTTTTTG - 3'), or exon 13 targeting BIN1 shRNA (5' –CCGGTGACGCATTTGTCCCTGAGATCTCGAGATCTGCAGGGACAAATGCGTCATTTTTG - 3') expressing lentivirus (Sigma) overnight. Post-viral infection, cardiomyocytes were cultured for 3 d before fixation for WGA labeled membrane intensity study. For actin experiments, fresh isolated cardiomyocytes were plated for 2 h, treated with 1 μM latrunculin A or 10 μM cytochalasin D overnight, and followed by PFA fixation and T-tubule labeling with Alexa647-conjugated WGA[50].

Membrane fluorescence labeling, immunofluorescence and Imaging

Freshly isolated ventricular cardiomyocytes from both WT and *Bin1* HT plasma membrane were incubated with 10 μM Di-8-ANNEPS for 20 min at room temperature. The cells were then washed with HBSS to remove the remaining dye and imaged with spinning disc confocal microscope. Di-8-ANEPPS labeled cells were excited with 488 nm laser and emitted fluorescence was collected through a 580 nm emission filter. For conjugated Wheat Germ Agglutinin (WGA) labeled membrane fluorescence, fresh isolated cardiomyocytes

were fixed with 4% PFA at room temperature for 30 min and labeled with Alexa-647 conjugated WGA at 4°C overnight followed by mounting in ProLong gold and imaged using spinning disc confocal microscope.

For all immunofluorescence, cells were fixed in methanol at −20 °C for 5 min. After fixation, cardiomyocytes were permeablized and blocked with 0.5% Triton X-100 and 5% NGS in PBS for 1hr at room temperature. The cells were incubated with mouse anti BIN1 exon 17 (99D, 1:50, Sigma) and rabbit anti Cav1.2 (1:50, Alomone); or rabbit anti BIN1 exon 13 (1:50, Anaspec) and mouse anti α-actinin (1:500, Abcam) overnight at 4°C. Exogenous protein expression after adenoviral infection was confirmed by anti-V5 (mouse anti-V5, Sigma, 1:500) labeling of the tagged protein introduced by adenovirus. After several washes with PBS post primary antibody incubation, cells were then incubated with goat anti-mouse IgG conjugated to AlexaFluor 488 and goat anti-rabbit IgG conjugated to AlexaFluor 555. Cells were then fixed and mounted with DAPI containing ProLong gold.

All imaging was performed on a Nikon Eclipse T*i* microscope with a 100 × 1.49 NA or 60 × 1.1 NA TIRF objectives and NIS Elements software. For BIN1 localization, isolated mouse cardiomyocytes were imaged at Z-depth increments of 0.5 μm. Deconvolution of images was performed using Autoquant software (Media Cybernetics). High-resolution cardiomyocyte images were obtained by using a spinning disc confocal unit (Yokogawa CSU10) with DPSS lasers (486, 561) generated from laser merge module 5 (Spectral applied research, CA) and captured by a high-resolution Cool SNAP HQ^2 camera (Photometrics).

For live-cell imaging of BIN1-GFP and LifeAct-mCherry, HeLa cells were transfected with BIN1+17-GFP or BIN1+13+17-GFP, along with co-transfection of LifeAct-mCherry. Co-transfected cells were imaged in regular HBSS (Gibco) using a 100 × 1.49 NA TIRF objective with spinning disc confocal microscopy. Live images were captured by using a high-resolution Cool SNAP HQ^2 camera (Photometrics).

Topography scans were obtained from freshly isolated adult cardiomyocytes using scanning ion conductance microscopy as described previously[51].

Electron Microscopy

For transmission electron microscopy study of in situ ventricular cardiomyocyte membrane ultrastructure, whole mouse hearts were perfused with fixative (2% paraformaldehyde / 2.5% Glutaraldehyde in 0.1 M Sodium cacodylate buffer, and 50 mM $CaCl_2$, pH 7.4) at 3 ml min^{-1} at room temperature for 15 min before being stored at 4 °C in fixative. T-tubules were labeled according to a previously established method[27]. Briefly, ultrathin heart tissue sections were cut by a Leica Ultracut S microtome and post-fixed in OsO4 (2% OsO4 + 0.8% $K_3Fe(CN)_6$ in 0.1 M cacodylate buffer (pH 7.4) (Sigma) and followed by uranyl acetate (EM Science) incubation before being dehydrated in ethanol and embedded in epon resin. Finally, tissue sections were imaged at 3,000×, 8,000× and 150,000× magnifications under a transmission electron microscope JEOL TEM1230 from the Electron Microscopy Core (EMC) of the Cell Sciences Imaging Facility (CSIF) at the Stanford University Medical Center. IMOD was used for three-dimensional reconstruction of TEM serial

sections, and a two-axis tomography of T-tubules was generated according to a previously established method[52,53].

Cardiomyocyte electrophysiology

Membrane capacitance and the macroscopic calcium (I_{Ca}) and the inward rectifying potassium channel mediated I_{K1} current were recorded by whole-cell voltage clamp of acutely isolated adult mouse cardiomyocytes. Patches were formed with borosilicate pipettes of 3–5 MΩ resistance. Data were acquired using an Axopatch 200-B patch-clamp amplifier and pClamp10 software (Molecular Devices). For membrane capacitance and I_{Ca} measurement, the internal solution contained (in mM) 130 CsCl, 10 NaCl, 10 tetraethylammonium chloride (TEA-Cl), 5 EGTA, 3 magnesium ATP and 10 HEPES, pH 7.2. For membrane capacitance measurement, the external solution contained (in mM) 140 NaCl, 5 CsCl, 2 $CaCl_2$, 1 $MgCl_2$, 10 glucose and 10 mM HEPES, pH 7.2. To estimate cell size, bright field images were taken before patch clamping through an Andor Clara DR-328G CCD camera in a Nikon TE2000U microscope. ImageJ software was used to measure the cell size. For I_{Ca} recording, the external solution contained (in mM) 140 TEA-Cl, 5 CsCl, 2 $CaCl_2$, 1 $MgCl_2$, 10 glucose and 10 HEPES, pH 7.2. To obtain the current-voltage relationship of I_{Ca}, test pulses were elicited from −90 mV to +50 mV with 10 mV increments. Both holding and repolarizing potentials were −90 mV.

To measure the diffusion barrier inside the cardiomyocyte T-tubules, I_{Ca} or I_{K1} was monitored while switching extracellular solutions with different calcium or potassium concentrations using a fast perfusion system (VC3-8xP pressured perfusion system, ALA Scientific Instruments). The protocol shown in Fig. 2a was used to measure calcium diffusion. If brief, the I_{Ca} was elicited by four conditioning pulses followed by a test pulse. Both conditioning and test pulses were from −80 to 0 mV for 200 ms. The delay between the conditioning pulses and the test pulse was gradually prolonged (with a step-wise 50 ms increment) during which the extracellular solution with 2 mM calcium was quickly switched to a solution with 5 mM EGTA. The change of I_{Ca} was normalized to the current of fourth conditioning pulse (I_{Max}) and fitted with one plateau followed by one phase exponential decay. A dead time of 124 ms due to dead volume was subtracted before fitting.

The intracellular solution for measuring the inward rectifying potassium channel mediated I_{K1} current contains (in mM): 100 potassium gluconate, 30 KCl, 1 $MgCl_2$, 1 EGTA, 3 sodium ATP, 10 Glucose, 10 HEPES, pH 7.3. The extracellular solution contains (in mM): 5 or 8.1 KCl, 140 NaCl, 1.8 $CaCl_2$, 1 $MgCl_2$, 0.2 $CdCl_2$, 10 Glucose, 10 HEPES, pH 7.3. Kinetics of I_{K1} changes following a quick switch of extracellular potassium concentration from 5 mM to 8.1 mM was constantly recorded by holding the cardiomyocytes at −80 mV. The kinetics was fitted with one plateau followed by one phase exponential decay. The dead time of the perfusion system between solution switches was 124 ms (measured by monitoring changes of junction potential, data not shown), and was subtracted from the initial delay time shown in Fig. 3.

All the experiments were performed at room temperature (22–24°C). Series resistance was compensated at 60–75% and monitored during the experiment. Recordings were filtered at 2–5 KHz and digitized at 10 KHz (Digidata 1440A, Molecular Devices). Clampfit 10

(Molecular Devices), Origin 7.5 (OriginLab) and Prism (Graphpad software) were used for data analysis.

Mathematical modeling of calcium diffusion in T-tubules

A set of 1 dimensional partial differential equations (PDEs) was developed to model calcium dynamics in the T-tubule. There are three time-dependent variables: the calcium concentration in the rapid diffusion zone, $c_1(x,t)$; number of calcium ions in the slow diffusion zone, $N_2(t)$; and the concentration of EGTA in the fast diffusion zone, $c_E(x,t)$ (see Fig. 2d). In our model, the slow diffusion zone can only exchange with the rapid diffusion zone at the distal end of the T-tubule farthest from the extracellular space. The equations are:

$$\frac{\partial c_1(x,t)}{\partial t} = \tau_{Ca} D_{Ca} \frac{\partial^2 c_1(x,t)}{\partial x^2} - \delta(x) \cdot k(c_1(x,t) - c_2(t)) - \sigma c_1 \cdot c_E$$

$$\frac{dN_2(t)}{dt} = k(c_1(0,t) - c_2(t))$$

$$\frac{\partial c_E(x,t)}{\partial t} = \tau_E D_E \frac{\partial^2 c_E(x,t)}{\partial x^2} - \sigma c_1 \cdot c_E$$

where k is the exchange rate between calcium in the slow and rapid diffusion zones, c_2 is the concentration of calcium in the slow diffusion zone ($c_2 = N_2/V_2$), σ is a rate constant for Ca^{2+} chelation by EGTA, D_{Ca}[54] and D_E[55] are the free diffusion constants of Ca^{2+} and EGTA, respectively, and τ_{Ca} and τ_E are tortuosity factors for Ca^{2+} and EGTA, respectively, that account for reduced diffusion in the T-tubule. The delta function, δ(x), indicates that compartment exchange only influences c_1 at the x = 0 end of the T-tubule.

The equations were solved in Matlab™ (2012a, The Mathworks, Natick, MA) using customized code. At each time step, the spatial diffusion terms for c_1 and c_E were first solved with a standard Crank-Nicholson tridiagonal scheme[56]. Next, $N_2(t)$, $c_1(0,t)$, and the chemical terms involving chelation, $\sigma c_i c_E$, were updated using a simple Euler method. The movement of ions across the boundary between slow and rapid zones involves geometric factors to properly convert the change in ion numbers in the slow diffusion space, ΔN_2, to a change in concentration in the rapid diffusion zone, Δc_1. Division of ΔN_2 by V_1, the volume of the first spatially, discretized element in the rapid diffusion zone, properly converts moles to concentration. V_1 is the cross-sectional area of the rapid diffusion zone of the T-tubule, A, times the spatial discretization along the length of the tubule, dx, such that $V_1 = Adx$. Initially, the calcium concentration was assumed to be uniform at 2 mM in both compartments, but the value was set to zero at the far right boundary, x = L (the T-tubule length), which corresponds to the bulk extracellular space. The right boundary was therefore treated as a Dirichlet boundary condition. The calcium concentration at the inner boundary, x = 0, was treated with a Neuman-type reflecting boundary condition. The EGTA concentration was initially set to zero in the rapid diffusion zone except where it was fixed to 2 mM at x = L. c_E was also treated with reflecting boundary conditions at x = 0 in the same manner as c_1. The convergence properties of the solution were investigated, and the

discretization values shown in Supplementary Table S1 for dt and dx provide well converged solutions.

The mathematical model was fit to the wildtype data in Fig. 2e using a Nelder-Mead Simplex method[56] provided in the Matlab™ package NMSMAX.m[57]. Six parameters indicated in Supplementary Table 1 were systematically varied, and the closeness of the modeled curve to the experimental data was calculated by using the following error function:

$$Error = -\sum_{i=1}^{N} |Y_i - Y_i^*|,$$

where i runs over all experimental data points, Y_i is the experimental value of the normalized current for point i, and Y^*_i is normalized calcium concentration in the slow diffusion zone corresponding to the time of point i. The search algorithm was run in 10–20 iterative rounds using the best fit from one round as the initial conditions for further runs. Each round was run for 200–1000 iterations. After fitting the model to the wildtype data, the diffusion barrier between compartments was removed by increasing the value of k by a factor of 100, and the normalized concentration in the slow diffusion zone was replotted without further fitting of the data.

All code will be provided upon request to M.G. (michael.grabe@ucsf.edu).

Optical mapping

Optical mapping was performed on mouse hearts, which were rapidly harvested after anesthesia and arrested in cold cardioplegia solution. The aorta was cannulated and retrogradely perfused with 37°C modified Tyrode solution (mmol L^{-1}: NaCl 120, $NaHCO_3$ 18, KH_2PO_4 1.2, $MgSO_4$ 1.2, glucose 11, $CaCl_2$ 1.8, sodium pyruvate 5, and Manitol 1, KCl 3.8), bubbled with 95% O_2/5% CO_2. Hearts were then placed in a temperature-controlled optical recording chamber (maintained at 37 °C) while electrocardiograms and perfusion pressures were measured continuously. Before optical recording, Tyrode solution containing voltage-sensitive dye di-4-ANEPPS (10 μl of 2.5 mM stock) was perfused through the hearts. Contractility was blocked using 5 μM blebbistatin. For studies of low and high extracellular K^+ perfusion, KCl concentration in Tyrode solution was adjusted to achieve a total K^+ concentration of 2.5 (low) or 8 (high) mM, as compared to normal 5 mM K^+ in the normal Tyrode solution.

The optical mapping system used has been previously described[58]. Briefly, action potentials were simultaneously recorded at 1,000 Hz with a 100 × 100 complementary metal oxide semiconductor (CMOS) camera with a 10 × 10 mm mapping field on the epicardium of the LV anterior wall. Fluorescence was excited using a 1,000-W tungsten-halogen light source with a filter of 530 nm and transmitted with an emission long-pass filter of 630 nm. Pacing was performed from two sites sutured with silver electrodes: one is on the apex of left ventricle with pacing cycle lengths (PCL) from 150 to 70 ms, and then with S1-S2 using a basic PCL of 150 ms and S2 decremented by 2 ms until the ventricular effective refractory

period was reached. After this, a train of programmed stimulation with up to three extra stimuli following a basic PCL of 150 ms and a burst pacing from 60 ms to 30 ms (decrement by 2 ms) were performed to induce ventricular arrhythmias. The other site is on the left atrium paced with simulated heart rates of 300, 400, 600, and 800 per min in order to induce ectopic ventricular beats.

Data analysis was performed using custom Matlab (Mathworks, Natick, MA) programs designed for analysis of optically recorded action potentials. Quantitative data were obtained from optically derived action potentials for each of the 10,000 pixels of the CMOS camera. Local activation was determined as the time point of maximum change in fluorescence over time ($dF\ dt^{-1}$) for each fluorescent signal in the array. Isochronal activation maps, conduction velocity were analyzed as described previously[59]. The action potential duration (APD) at 80% repolarization (APD_{80}) was determined as the time difference between the take-off potential and the point during repolarization at 20% of the maximal action potential amplitude.

In vivo cardiac electrophysiology studies in adult mice

Invasive intracardiac electrophysiology was studied in young adult mice (8 week old) following a previously established protocol with some modification[32]. Mice were anesthetized with 1% isofluorane in 100% oxygen, body temperature was maintained at 37°C by a heating pad, and respiration was maintained using a respirator connected to an endotracheal tube placed into mouse trachea. Electrocardiograms (EKG) were recorded using PowerLab (ADInstruments) during the whole experimental procedure. Upon lateral thoracotomy, the heart was visualized, and two platinum electrodes were placed on the apex of the left ventricle for pacing. A constant current stimulus isolator (FE180, ADInstruments, Colorado Springs, CO) was used to deliver pacing currents, which was interfaced with a software-driven programmed electrical stimulator (LabChart Pro, ADInstruments, Colorado Springs, CO). Pacing thresholds were then determined and stimulation was delivered at 0.30.4 ms pulse width, at twice of the capture threshold. Standard triple extrastimulation were performed. A drive cycle length of 80ms (S1) followed by S2 decremented by 2 ms until the ventricular effective refractory period was reached. After this, a train of programmed stimulation with three extra stimuli following S1 (S1–S4) was performed and repeated every 10 s for 10 min to determine the incidence and frequency of induced VT. After baseline experiment, isoproterenol (0.1 mg kg^{-1}) was injected into left ventricle and 10 min were allowed to elapse for stabilization of heart rate before the same S1–S4 pacing protocol was repeated. Non-sustained VT was defined as 4–9 consecutive beats and sustained VT was defined as >9 QRS complexes not preceded by superventricular activity[31]. LabChart was used for data analysis.

In vitro actin complex formation using heart lysates

Adult mouse hearts were perfused through aorta to remove blood and lysed in actin polymerization buffer (in mM, 150 KCl, 20 HEPES, 2 MgCl2, 2 K2HPO4, 1% NP40, pH7.4 with halt protease inhibitor). Following a10 minute incubation on ice, the lysate was ultra-centrifuged for 1 h at 170,000g at 4°C in a bench top Beckman type Ti-50 fixed angle rotor to remove endogenous F-actin polymers. The F-actin free supernatant was collected and

divided equally into four aliquots. Each of the aliquots was then supplemented with various GST-BIN1 isoform coated glutathione beads (BIN1, BIN1+13, BIN1+17, and BIN1+13+17), which were prepared fresh by incubating glutathione beads with lysates of FT293 cells overexpressing different GST-BIN1 isoform (2 h incubation at 4 °C). The F-actin free heart lysates supplemented with BIN1 beads were then rotated head-to-toe overnight (16 h) at 4 °C in the present of 25 μM phallodin and 100 μM ATP, allowing in vitro actin polymerization. Then the BIN1 coated beads were spun down and washed three times in actin polymerization buffer at 4 °C. Finally, the BIN1 and its associated protein complex were eluted from the beads in SDS-PAGE sample buffer (70 °C for 10 min) and resolved by gel electrophoresis.

Pull down between GST-BIN1 isoforms and α-actinin or N-WASP

For GST-BIN1 mediated pull down of α-actinin, adult hearts were lysed in 0.5% NP40 buffer (in mM, 150 KCl, 20 HEPES, 2 $MgCl_2$, 2 K_2HPO4, 1 DTT, 1 NaF, 0.1 Na_3VO_4, 0.5% NP40, pH7.4 with halt protease inhibitor). The lysates were then divided equally into five portions and incubated with purified GST-GFP, GST-BIN1, GST-BIN1+13, GST-BIN1+17, or GST-BIN1+13+17 coated glutathione beads prepared as stated in the last section. The lysates were rotated head-to-toe at 4 °C for 2 h to allow protein complex formation. BIN1 protein complex attached beads were then washed and eluted in 4× sample buffer (70°C for 10 min). The eluted samples were resolved by Western blot for the detection of α-actinin and GST-BIN1.

For BIN1 pulldown of N-WASP, HeLa cells overexpressing N-WASP-V5 and GST-BIN1 protein isoforms were lysed and incubated with glutathione beads at 4 °C for 30 min to pull down GST fusion protein complex.

In vitro actin polymerization assay

Actin Polymerization Biochem Kit, purified Arp2/3 protein complex, and purified VCA domain of N-WASP were obtained from Cytoskeleton. GST fused N-WASP and BIN1 protein isoforms were purified by glutathione beads pulldown followed by elution with 5mM glutathione. The protein was then concentrated and washed with Amicon concentrator to reach a final concentration of 10 μM in 100 mM Tris (pH 7.4) buffer to be compatible with actin assay. The manufactual actin polymerization protocol was optimized using 0.2 mg ml^{-1} 100% pyrene labeled actin supplemented with 60 nM Arp2/3 protein complex and N-WASP (200 nM) in the presence of control GST-GFP protein or 1 μM of BIN1 isoforms. Pyrene-actin alone (supplemented with GST-GFP for a similar total protein concentration) was used as the negative control. For positive control, N-WASP was replaced with 200 nM purified VCA domain of N-WASP. Baseline pyrene fluorescence (excitation 360 nm and emission 410 nm) and 90 min polymerization kinetics were recorded with a FlexStation 3 Microplate Reader (Molecular Devices). SoftMax Pro 5.4.5 (Molecular Device) was used for data analysis including Vmax calculation.

Signal Processing and Statistical Analysis

Fluorescence intensity profiles were generated by ImageJ. Prism 5 (GraphPad) software was used for statistical analysis. For comparison between two groups, paired or unpaired two-tail

student's *t*-test was performed. For comparison among three and more treatment groups, one-way ANOVA followed by Dunnet post-test was performed. For I_{Ca} and I_{K1} decay kinetics, the curves were fit with one-plateau followed by one-phase exponential decay in Prism. For comparison of VT incidence among three genetic groups, chi-sqaure test was used, and for comparison of VT frequency before and after isoproterenol among three genetic groups, two-way ANOVA was used.

Supplementary Material

Refer to Web version on PubMed Central for supplementary material.

ACKNOWLEDGMENTS

This work was supported by US National Institutes of Health grants R01 HL094414 (R.M.S.), R37 MH065334 (L.Y.J.), R21 GM100224 (M.G.), T32 HL116273 (S.Z.) and K99/R00 HL109075-01A1 (T.T.H.), and American Heart Association (S.Z., R.M.S.). L.Y.J. is a Howard Hughes Medical Institute investigator. We thank E. Cingolani for helpful advice on designing the in vivo pacing protocol, D. Laury-Kleintop and G.C. Prendergast from Lankenau Institute for Medical Research for *Bin1-loxP* mice, J. Mulholland and J. J. Perrino for TEM imaging at the Electron Microscopy Core (EMC, directed by J. Mulholland) of the Cell Sciences Imaging Facility (CSIF) at the Stanford University Medical Center, J. Smyth and R. Wirka for helpful discussions, and T.S. Fong and T. Hitzeman for technical assistance.

REFERENCES

1. Soeller C, Cannell MB. Examination of the transverse tubular system in living cardiac rat myocytes by 2-photon microscopy and digital image-processing techniques. Circ Res. 1999; 84:266–275. [PubMed: 10024300]
2. Brette F, Orchard C. T-tubule function in mammalian cardiac myocytes. Circ Res. 2003; 92:1182–1192. [PubMed: 12805236]
3. Cheng H, Lederer WJ, Cannell MB. Calcium sparks: elementary events underlying excitation-contraction coupling in heart muscle. Science. 1993; 262:740–744. [PubMed: 8235594]
4. Bers DM. Cardiac excitation-contraction coupling. Nature. 2002; 415:198–205. [PubMed: 11805843]
5. Pasek M, Simurda J, Christe G. The functional role of cardiac T-tubules explored in a model of rat ventricular myocytes. Philos Transact A Math Phys Eng Sci. 2006; 364:1187–1206.
6. Lederer WJ, Niggli E, Hadley RW. Sodium-calcium exchange in excitable cells: fuzzy space. Science. 1990; 248:283. [PubMed: 2326638]
7. Shepherd N, McDonough HB. Ionic diffusion in transverse tubules of cardiac ventricular myocytes. Am J Physiol. 1998; 275:H852–H860. [PubMed: 9724289]
8. Swift F, Stromme TA, Amundsen B, Sejersted OM, Sjaastad I. Slow diffusion of K+ in the T tubules of rat cardiomyocytes. J Appl Physiol. 2006; 101:1170–1176. [PubMed: 16763106]
9. Parfenov AS, Salnikov V, Lederer WJ, Lukyanenko V. Aqueous diffusion pathways as a part of the ventricular cell ultrastructure. Biophys J. 2006; 90:1107–1119. [PubMed: 16284268]
10. Pasek M, Simurda J, Orchard CH. Role of t-tubules in the control of trans-sarcolemmal ion flux and intracellular Ca2+ in a model of the rat cardiac ventricular myocyte. Eur Biophys J. 2012; 41:491–503. [PubMed: 22466899]
11. Pasek M, Simurda J, Orchard CH, Christe G. A model of the guinea-pig ventricular cardiac myocyte incorporating a transverse-axial tubular system. Prog Biophys Mol Biol. 2008; 96:258–280. [PubMed: 17888503]
12. Lyon AR, et al. Loss of T-tubules and other changes to surface topography in ventricular myocytes from failing human and rat heart. Proc Natl Acad Sci U S A. 2009; 106:6854–6859. [PubMed: 19342485]

13. Wei S, et al. T-tubule remodeling during transition from hypertrophy to heart failure. Circ Res. 2010; 107:520–531. [PubMed: 20576937]
14. Wagner E, et al. Stimulated emission depletion live-cell super-resolution imaging shows proliferative remodeling of T-tubule membrane structures after myocardial infarction. Circ Res. 2012; 111:402–414. [PubMed: 22723297]
15. Aiba T, Tomaselli GF. Electrical remodeling in the failing heart. Curr Opin Cardiol. 2010; 25:29–36. [PubMed: 19907317]
16. Sipido KR. Calcium overload, spontaneous calcium release, and ventricular arrhythmias. Heart Rhythm. 2006; 3:977–979. [PubMed: 16876751]
17. Lee E, et al. Amphiphysin 2 (Bin1) and T-tubule biogenesis in muscle. Science. 2002; 297:1193–1196. [PubMed: 12183633]
18. Hong TT, et al. BIN1 Localizes the L-Type Calcium Channel to Cardiac T-Tubules. PLoS Biol. 2010; 8:e1000312. [PubMed: 20169111]
19. Hong TT, et al. BIN1 is reduced and Cav1.2 trafficking is impaired in human failing cardiomyocytes. Heart Rhythm. 2012; 9:812–820. [PubMed: 22138472]
20. Lyon AR, et al. Plasticity of surface structures and beta(2)-adrenergic receptor localization in failing ventricular cardiomyocytes during recovery from heart failure. Circ Heart Fail. 2012; 5:357–365. [PubMed: 22456061]
21. Bohm J, et al. Case report of intrafamilial variability in autosomal recessive centronuclear myopathy associated to a novel BIN1 stop mutation. Orphanet J Rare Dis. 2010; 5:35. [PubMed: 21129173]
22. Muller AJ, et al. Targeted disruption of the murine Bin1/Amphiphysin II gene does not disable endocytosis but results in embryonic cardiomyopathy with aberrant myofibril formation. Mol Cell Biol. 2003; 23:4295–4306. [PubMed: 12773571]
23. Agah R, et al. Gene recombination in postmitotic cells. Targeted expression of Cre recombinase provokes cardiac-restricted, site-specific rearrangement in adult ventricular muscle in vivo. J Clin Invest. 1997; 100:169–179. [PubMed: 9202069]
24. Goonasekera SA, et al. Decreased cardiac L-type Ca(2)(+) channel activity induces hypertrophy and heart failure in mice. J Clin Invest. 2012; 122:280–290. [PubMed: 22133878]
25. Kawai M, Hussain M, Orchard CH. Excitation-contraction coupling in rat ventricular myocytes after formamide-induced detubulation. Am J Physiol. 1999; 277:H603–H609. [PubMed: 10444485]
26. Hepler PK. Membranes in the mitotic apparatus of barley cells. J Cell Biol. 1980; 86:490–499. [PubMed: 7400216]
27. Franzini-Armstrong C. Simultaneous maturation of transverse tubules and sarcoplasmic reticulum during muscle differentiation in the mouse. Dev Biol. 1991; 146:353–363. [PubMed: 1864461]
28. Komukai K, Brette F, Yamanushi TT, Orchard CH. K(+) current distribution in rat sub-epicardial ventricular myocytes. Pflugers Arch. 2002; 444:532–538. [PubMed: 12136273]
29. Pasek M, et al. Quantification of t-tubule area and protein distribution in rat cardiac ventricular myocytes. Prog Biophys Mol Biol. 2008; 96:244–257. [PubMed: 17881039]
30. Shaw RM, Rudy Y. Electrophysiologic effects of acute myocardial ischemia. A mechanistic investigation of action potential conduction and conduction failure. Circ Res. 1997; 80:124–138. [PubMed: 8978331]
31. Mathur N, et al. Sudden infant death syndrome in mice with an inherited mutation in RyR2. Circ Arrhythm Electrophysiol. 2009; 2:677–685. [PubMed: 20009080]
32. Kannankeril PJ, et al. Mice with the R176Q cardiac ryanodine receptor mutation exhibit catecholamine-induced ventricular tachycardia and cardiomyopathy. Proc Natl Acad Sci U S A. 2006; 103:12179–12184. [PubMed: 16873551]
33. Marban E, Robinson SW, Wier WG. Mechanisms of arrhythmogenic delayed and early afterdepolarizations in ferret ventricular muscle. J Clin Invest. 1986; 78:1185–1192. [PubMed: 3771791]
34. Tian Q, et al. Functional and morphological preservation of adult ventricular myocytes in culture by sub-micromolar cytochalasin D supplement. J Mol Cell Cardiol. 2012; 52:113–124. [PubMed: 21930133]

35. Yamada H, et al. Dynamic interaction of amphiphysin with N-WASP regulates actin assembly. J Biol Chem. 2009; 284:34244–34256. [PubMed: 19759398]
36. Gaur N, Rudy Y, Hool L. Contributions of ion channel currents to ventricular action potential changes and induction of early afterdepolarizations during acute hypoxia. Circ Res. 2009; 105:1196–1203. [PubMed: 19875728]
37. Kim JM, Bursac N, Henriquez CS. A computer model of engineered cardiac monolayers. Biophys J. 2010; 98:1762–1771. [PubMed: 20441739]
38. Gez LS, Hagalili Y, Shainberg A, Atlas D. Voltage-driven Ca(2+) binding at the L-type Ca(2+) channel triggers cardiac excitation-contraction coupling prior to Ca(2+) influx. Biochemistry. 2012; 51:9658–9666. [PubMed: 23145875]
39. Taylor MJ, Perrais D, Merrifield CJ. A high precision survey of the molecular dynamics of mammalian clathrin-mediated endocytosis. PLoS Biol. 2011; 9:e1000604. [PubMed: 21445324]
40. Butler MH, et al. Amphiphysin II (SH3P9-BIN1), a member of the amphiphysin/Rvs family, is concentrated in the cortical cytomatrix of axon initial segments and nodes of ranvier in brain and around T tubules in skeletal muscle. J Cell Biol. 1997; 137:1355–1367. [PubMed: 9182667]
41. Bohm J, et al. Altered splicing of the BIN1 muscle-specific exon in humans and dogs with highly progressive centronuclear myopathy. PLoS Genet. 2013; 9:e1003430. [PubMed: 23754947]
42. Ge K, et al. Mechanism for elimination of a tumor suppressor: aberrant splicing of a brain-specific exon causes loss of function of Bin1 in melanoma. Proc Natl Acad Sci U S A. 1999; 96:9689–9694. [PubMed: 10449755]
43. Sakamuro D, Elliott KJ, Wechsler-Reya R, Prendergast GC. BIN1 is a novel MYC-interacting protein with features of a tumour suppressor. Nat Genet. 1996; 14:69–77. [PubMed: 8782822]
44. Elliott K, et al. Bin1 functionally interacts with Myc and inhibits cell proliferation via multiple mechanisms. Oncogene. 1999; 18:3564–3573. [PubMed: 10380878]
45. Kashef F, et al. Ankyrin-B protein in heart failure: identification of a new component of metazoan cardioprotection. J Biol Chem. 2012; 287:30268–30281. [PubMed: 22778271]
46. Beuckelmann DJ, Nabauer M, Erdmann E. Alterations of K+ currents in isolated human ventricular myocytes from patients with terminal heart failure. Circ Res. 1993; 73:379–385. [PubMed: 8330380]
47. Smyth JW, et al. Actin cytoskeleton rest stops regulate anterograde traffic of connexin 43 vesicles to the plasma membrane. Circ Res. 2012; 110:978–989. [PubMed: 22328533]
48. O'Connell TD, Rodrigo MC, Simpson PC. Isolation and culture of adult mouse cardiac myocytes. Methods Mol Biol. 2007; 357:271–296. [PubMed: 17172694]
49. Hattori F, et al. Nongenetic method for purifying stem cell-derived cardiomyocytes. Nat Methods. 2010; 7:61–66. [PubMed: 19946277]
50. Leach RN, Desai JC, Orchard CH. Effect of cytoskeleton disruptors on L-type Ca channel distribution in rat ventricular myocytes. Cell Calcium. 2005; 38:515–526. [PubMed: 16137761]
51. Novak P, et al. Nanoscale live-cell imaging using hopping probe ion conductance microscopy. Nat Methods. 2009; 6:279–281. [PubMed: 19252505]
52. Kremer JR, Mastronarde DN, McIntosh JR. Computer visualization of three-dimensional image data using IMOD. J Struct Biol. 1996; 116:71–76. [PubMed: 8742726]
53. Mastronarde DN. Dual-axis tomography: an approach with alignment methods that preserve resolution. J Struct Biol. 1997; 120:343–352. [PubMed: 9441937]
54. Shorten PR, Soboleva TK. Anomalous ion diffusion within skeletal muscle transverse tubule networks. Theor Biol Med Model. 2007; 4:18. [PubMed: 17509153]
55. Kits KS, de Vlieger TA, Kooi BW, Mansvelder HD. Diffusion barriers limit the effect of mobile calcium buffers on exocytosis of large dense cored vesicles. Biophys J. 1999; 76:1693–1705. [PubMed: 10049349]
56. Press, W. Numerical Recipes: The Art of Scientific Computing. Cambridge University Press; 2007.
57. Higham NJ. Optimization by direct search in matrix computations. SIAM J. Matrix Anal. Appl. 1993; 14:317–333.

58. Nguyen DT, Ding C, Wilson E, Marcus GM, Olgin JE. Pirfenidone mitigates left ventricular fibrosis and dysfunction after myocardial infarction and reduces arrhythmias. Heart Rhythm. 2010; 7:1438–1445. [PubMed: 20433946]

59. Salama G, Kanai A, Efimov IR. Subthreshold stimulation of Purkinje fibers interrupts ventricular tachycardia in intact hearts. Experimental study with voltage-sensitive dyes and imaging techniques. Circ Res. 1994; 74:604–619. [PubMed: 8137497]

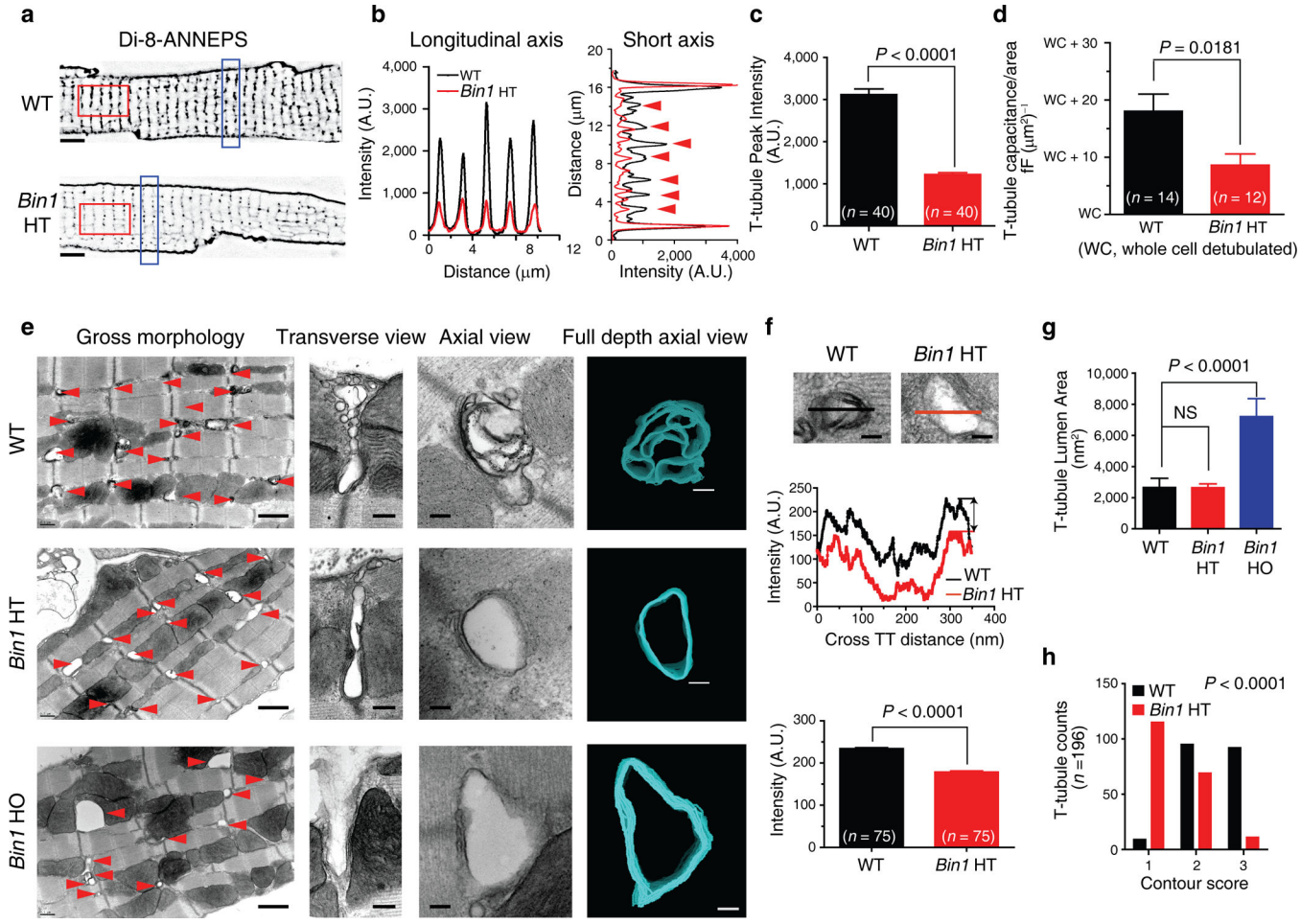

Figure 1.

Cardiomyocyte T-tubules are densely folded by BIN1. (**a–b**) Representative confocal images (**a**, scale bars: 5 μm) and the fluorescent profiles (**b**) of live WT and *Bin1* HT cardiomyocytes labeled with Di-8-ANNEPS. (**c**) Quantification of T-tubules peak intensity. (n = 40 from 4–5 cells, $P < 0.0001$). (**d**) Cell size normalized membrane capacitance in WT (n = 14) and *Bin1* HT (n = 12) cardiomyocytes ($P = 0.0181$). WC indicates reported whole cell capacitance without T-tubules. (**e**) 2D transmission electron microscope (TEM) images (Left to right: gross morphology, transverse cross section, and axial cross section) and 3D electron tomography images (right) of WT and *Bin1* HT heart sections. Scale bars (left to right): 1 μm, 250 nm, 100 nm, and 100 nm. (**f**) Electron density profiles (middle) across individual T-tubules marked by the lines in the images above, with average T-tubule electron density in the bottom (n = 75, $P < 0.0001$). (**g**) T-tubule lumen area of axial cross sections (n = 80, $P < 0.0001$). (**h**) Cardiomyocyte T-tubule contour score (1, circular shape and no folds and spatial complexity; 2, non-circular shape and no folds and spatial complexity; or 3, multiple folds with spatial complexity) distribution (n = 196, $P < 0.0001$). Data are presented as mean ± SEM, cardiomyocytes are from three mice per genotype, and six left ventricular sections from three hearts per genotype were used for TEM analysis. Student's t-test and one way-ANOVA were used for statistical analysis.

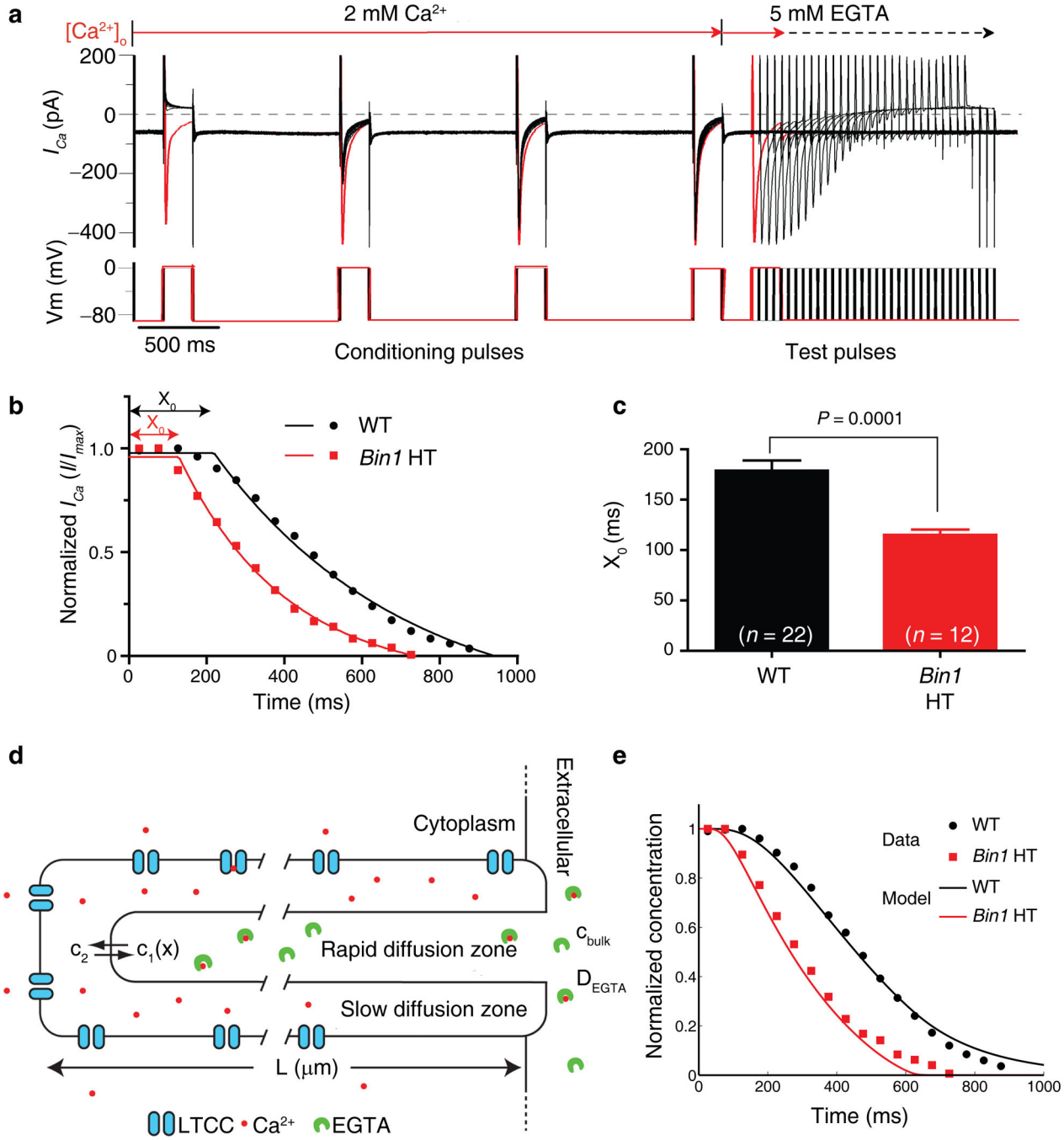

Figure 2.

Bin1 deletion increases extracellular Ca^{2+} diffusion. (**a**) Representative patch clamp recording of the LTCC mediated I_{Ca} from a WT cardiomyocyte in response to quick change from 2 mM extracellular calcium solution to calcium free 5 mM EGTA solution. (**b**) Kinetics of I_{Ca} current changes using the protocol described in (**a**) were fitted with one plateau followed by one phase exponential decay. X_0 is the initial delay before I_{Ca} decays. (**c**) Comparison of X_0 for WT and *Bin1* HT. Data are presented as mean ± SEM, $P = 0.0001$ by student's *t*-test (cardiomyocytes are from 3 mice for each genotype). (**d**) A diagram

describing the salient features of a mathematical model for calcium diffusion. (**e**) Kinetics of I_{Ca} current decay computed using the model in (**d**). The normalized calcium concentration in the slow diffusion zone serves as a surrogate for the calcium current since it is directly related to the inward Ca^{2+} driving force. The model of WT T-tubules containing a slow diffusion zone matches the experimental data (black curve – model, black circles – data). Removal of the diffusion barrier at the left side of the T-tubule in (**a**) results in a shorter initial delay as observed in the *Bin1* HT experiments (red curve – model, red squares – data).

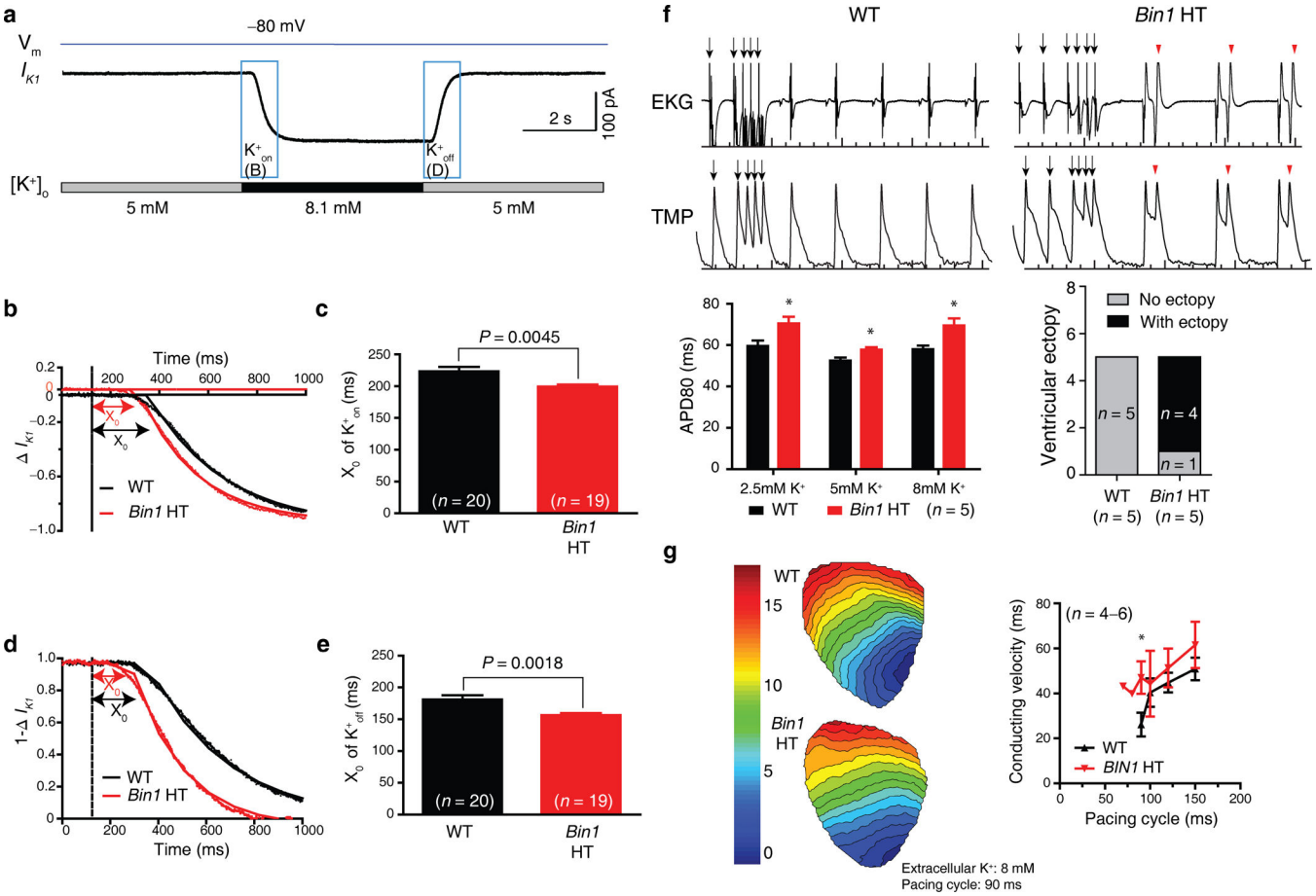

Figure 3.

Bin1 deletion increases extracellular K^+ diffusion, prolonging action potential duration and increasing ventricular ectopy. (**a**) Representative patch clamp recording of I_{K1} current changes when quickly switching extracellular potassium concentration in a wildtype (WT) cardiomyocyte. (**b**) Kinetics of I_{K1} during K^+_{on} in WT and *Bin1* HT cardiomyocytes (dotted line, dead volume time of 124 ms). (**c**) Comparison of the initial delay X_0 of K^+_{on} for WT (n = 20) and *Bin1* HT (n = 19) cardiomyocytes (P = 0.0045). (**d**) Kinetics of I_{K1} during K^+_{off} ($1-\Delta I_{K1}$) in WT and *Bin1* HT cardiomyocytes. (**e**) Comparison of X_0 of K^+_{off} for WT (n = 20) and *Bin1* HT (n = 19) cardiomyocytes (P = 0.0018). (**f**) Top: representative tracings of EKG (top) and TMP (transmembrane potential, bottom) from isolated and langendorff perfused WT (left) and *Bin1* HT (right) hearts. Bottom: Action potential duration (APD80) is always prolonged in *Bin1* HT hearts whether subjected to low (2.5 mM), normal (5 mM), and high (8 mM) potassium solution (left), and ventricular ectopy is increased in *Bin1* HT hearts (right, incidence of arrhythmias during physiological buffer perfusion). (**g**) Ventricular activation map (left) and conduction velocity (right) of WT and *Bin1* HT hearts subjected to high potassium (8 mM) perfusion (*, $P < 0.05$). Data are presented as mean ± SEM and cardiomyocytes are from three mice for each genotype, student's *t*-test was used for statistical analysis.

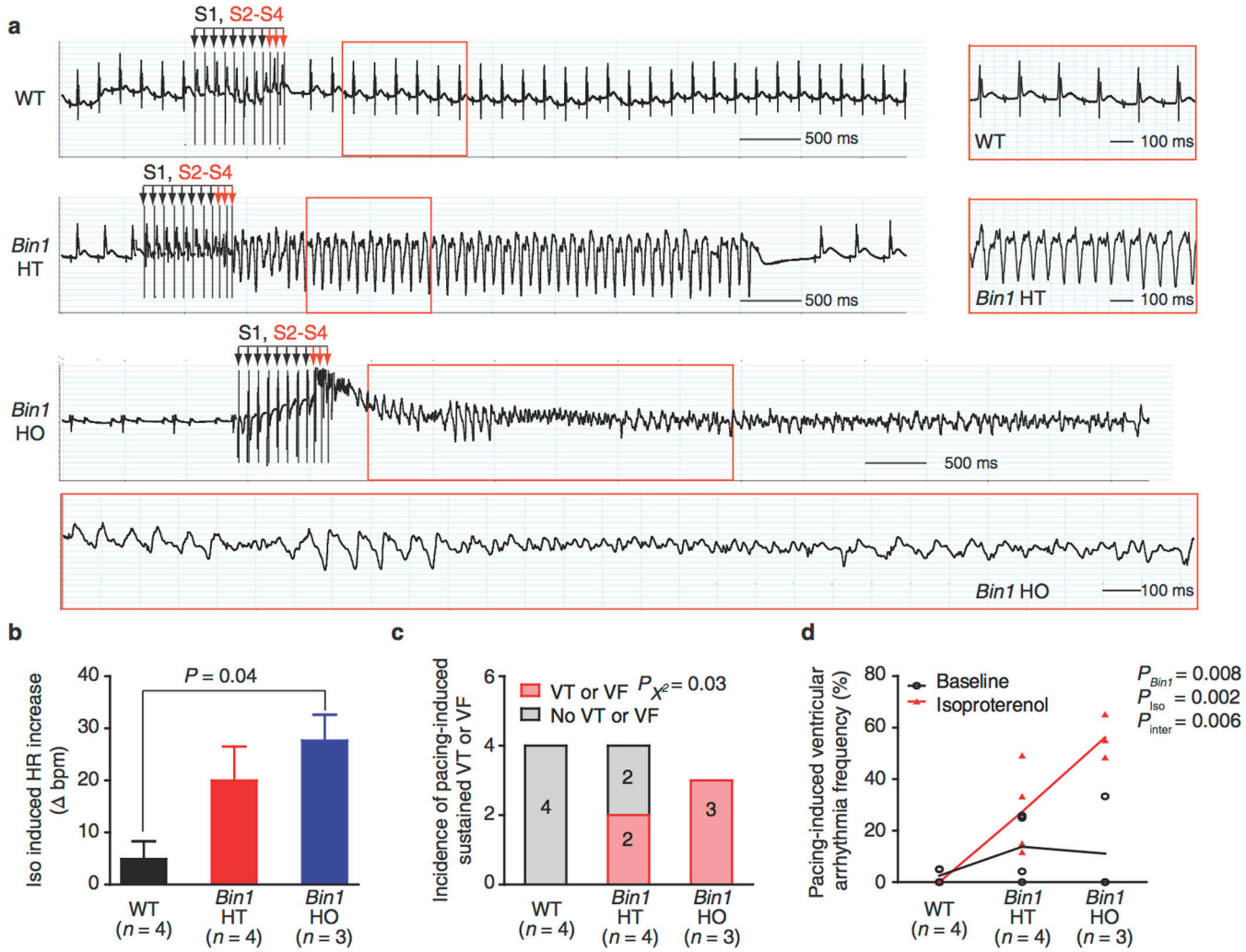

Figure 4.

Ventricular arrhythmias induced by pacing and beta adrenergic activation with isoproterenol. (**a**) Representative recordings of EKG following a S1–S4 stimulation protocol. Normal sinus node beats resume immediately following pacing in WT mice (top panel), sustained monomorphic ventricular tachycardia (4.5 s) was induced in *Bin1* HT mice (middle panel), sustained polymorphic ventricular tachycardia (VT) alternating with ventricular fibrillation (VF) (>20s) was induced in *Bin1* HO mice (bottom panel). (**b**) Heart rate increase (ΔHR) in response to isoproterenol was analyzed and compared among the three groups (mean ± SEM, n = 3–4, P = 0.04 by one-way ANOVA). (**c**) Incidence of sustained VT (>9 QRS) or VF in each group (n = 3–4, P = 0.03 by chi-square). (**d**) The frequency of ventricular arrhythmias before and after isoproterenol treatment was quantified in each group (n = 3–4, P < 0.01 by two-way ANOVA).

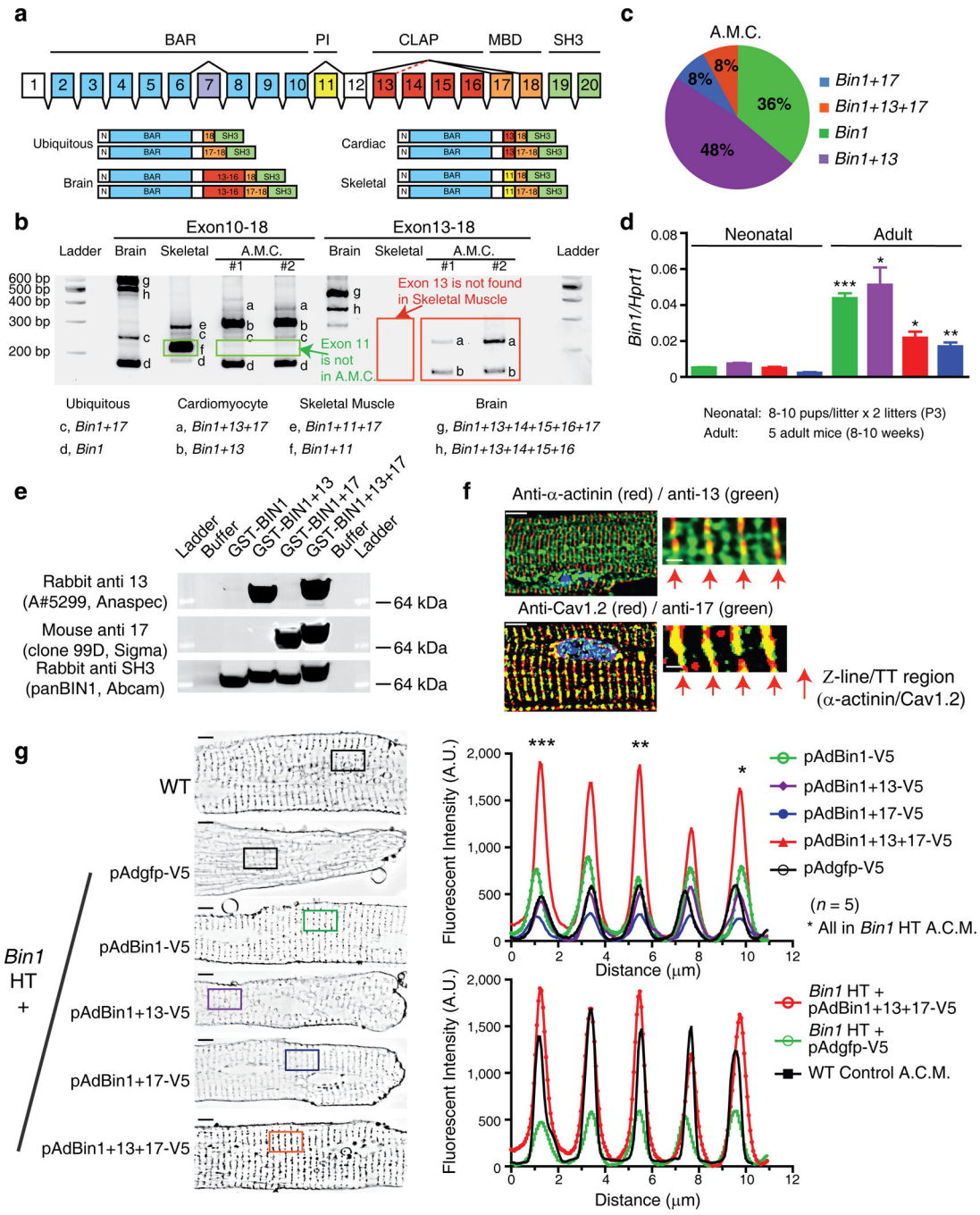

Figure 5.

Adult mouse cardiomyocytes express four *Bin1* splice variants. (**a**) Cartoon of *Bin1* exons and the splice variants we found in adult mouse cardiomyocytes. BAR, Bin–Amphiphysin–Rvs domain; PI, phosphoinositide binding domain; CLAP, clathrin / AP2 binding region; MDB, myc-binding domain; SH3, SRC Homology 3 domain. (**b**) Four *Bin1* splice variants with alternative inclusion of exon 13 and 17 are detected in adult mouse cardiomyocytes (A.M.C.) using PCR detection with primer sets flanking exon 10–18 or exon 13–18. (**c**) The percent of each *Bin1* variants in adult mouse cardiomyocytes after subcloning and

sequencing using PCR primer sets flanking exon 10–18. (**d**) Quantitative rtPCR analysis of each *Bin1* variants (*Bin1/HPRT1*) in purified neonatal cardiomyocytes (P3, $n = 2$ litters with 8–10 pups each) and isolated adult mouse cardiomyocytes ($n = 5$ mice). (**e**) Western blot analysis confirms the antibody specificity of anti-exon 17 (clone 99D, Sigma) and anti-exon 13 (A#5299, Anaspec) BIN1 antibodies. All four BIN1 isoforms are detected by panBIN1 antibody (rabbit anti BIN1 SH3 domain). (**f**) Immunofluorescence of anti-exon 17 and anti-exon 13 labeling (red arrow, Z-line/TT region by α-actinin or Cav1.2 co-labeling) in adult mouse cardiomyocytes. (**g**) Representative confocal images (left, scale bars: 5 μm) and fluorescent profiles (right) of Di-8-ANNEPS membrane labeling in WT and *Bin1* HT cardiomyocytes over-expressing GFP, BIN1, BIN1+13, BIN1+17, or BIN1+13+17 ($n = 5$ cells). Data are presented as mean +/− SEM. *, $P < 0.05$; **, $P < 0.01$, and ***, $P < 0.001$ by student's *t*-test or two-way ANOVA.

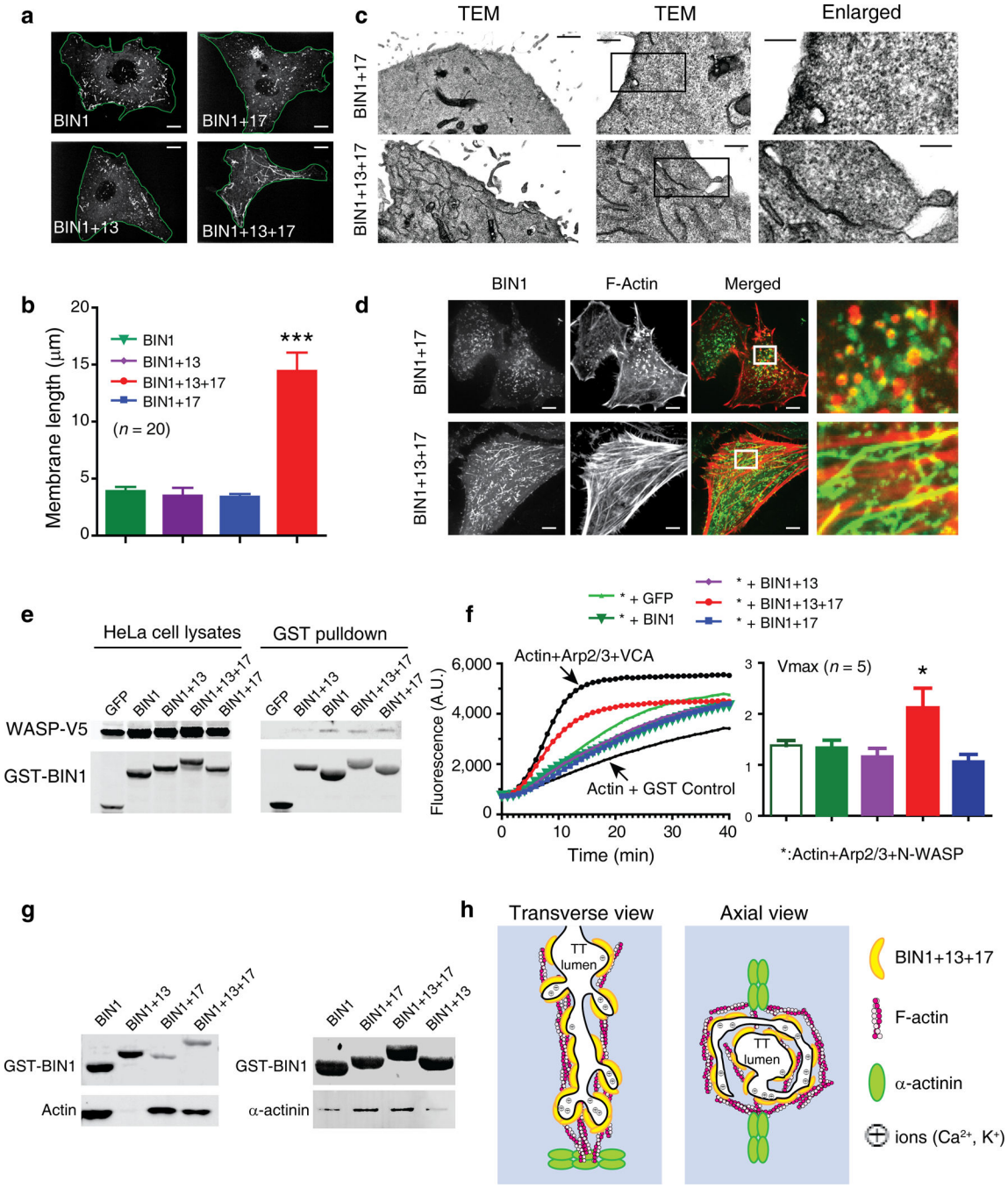

Figure 6.

BIN1+13+17 uses F-actin to connect to Z-disc α-actinin. **(a–b)** HeLa cells expressing GFP tagged BIN1, BIN1+13, BIN1+17, and BIN1+13+17 (scale bars: 10 μm) (**a**), with the length of folds like structure (linear streaks) quantified in (**b**). (Mean ± SEM; *n* = 20 folds from 5 cells; *** indicates $P < 0.001$ by one-way ANOVA). (**c**) TEM confirms that BIN1+13+17 but not BIN1+17 induces elongated membrane folds in HeLa cells. Scale bars: 1 μm (left) and 0.5 μm (right two panels). (**d**) HeLa cells expressing isoforms of GFP-BIN1 (green) and LifeAct-mCherry (red) (scale bars: 10 μm). (**e**) GST pulldown of GST-BIN1 isoforms and

N-WASP-V5 in HeLa cells. (**f**) In vitro pyrene-actin polymerization assay using purified Arp2/3, N-WASP and BIN1 isoforms. Left, representative tracing of actin polymerization kinetics. Right, the Vmax data of polymerization kinetics. Data are presented as mean ± SEM ($n = 5$, * indicates $P < 0.05$ by one-way ANOVA). The negative control contains pyrene-actin alone with a GST control protein (GST-GFP, bottom black line indicated by the bottom arrow), the positive control contains pyrene-actin supplemented with Arp2/3 and VCA (active domain of N-WASP, top black line indicate by the top arrow), and the rest samples contain pyrene-actin supplemented with Arp2/3, N-WASP with GST-GFP or 1 μM GST-BIN1 isoforms. (**g**) Purified GST-BIN1 fusion protein pre-coated glutathione beads were added to adult heart lysates for pulldowns of α-actinin (right) or F-actin (left). (**h**) Schematic illustration of BIN1+13+17 forming an extracellular ionic diffusion barrier inside T-tubules.